ACS APPLIED MATERIALS & INTERFACES

Research Article

www.acsami.org

Ultrafast Synthesis of Yolk-Shell and Cubic NiO Nanopowders and Application in Lithium Ion Batteries

Seung Ho Choi and Yun Chan Kang*

Department of Chemical Engineering, Konkuk University, 1 Hwayang-dong, Gwangjin-gu, Seoul 143-701, Korea

Supporting Information

ABSTRACT: A continuous one-pot method was employed to synthesize yolk-shell and single-crystalline cubic NiO powders in a few seconds. Submicrometer-sized NiO yolk-shell particles were prepared by spray pyrolysis at 900 °C. Single-crystalline cubic NiO nanopowders were prepared by one-pot flame spray pyrolysis from NiO vapors. Particle surface areas of the yolk-shell and single-crystalline cubic NiO powders as obtained using the Brunauer–Emmett–Teller method were 8 and 5 m^2 g^{-1}, respectively. The mean crystallite sizes of the yolk-shell-structured and cubic NiO powders were 50 and 80 nm, respectively. The yolk-shell and single-crystalline cubic NiO powders delivered discharge capacities of 951 and 416 mA h g^{-1}, respectively, after 150 cycles, and the corresponding capacity retentions measured after the first cycle were 106 and 66%, respectively. The yolk-shell-structured NiO powders showed rate performance better than that of the single-crystalline cubic NiO nanopowders. Even at a high current density of 1 A g^{-1}, the discharge capacity of the yolk-shell-structured NiO powders was as high as 824 mA h g^{-1} after 50 cycles, in which the current densities were increased stepwise.

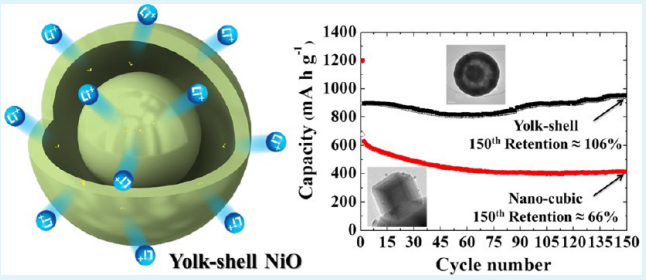

KEYWORDS: *yolk shell, nanocubic, anode material, lithium ion battery, spray pyrolysis, flame spray pyrolysis*

INTRODUCTION

Transition-metal oxides with high theoretical capacities have attracted enormous attention as anode materials for lithium ion batteries (LIBs) in place of the conventional carbon-based materials.[1−5] However, most transition-metal oxides suffer from poor cycle performance because of their low electrical conductivity and the large change in volume during cycling (i.e., Li^+ insertion and/or extraction).[2−5] Therefore, transition-metal oxide powders with varied structures such as hollow, yolk shell, and nanotubes have been developed to achieve high reversible capacity, good rate capability, and enhanced cycling performance.[6−15] The intrinsic properties of nanostructured materials are mainly affected by their morphology and crystallinity. Because of their unique properties, yolk-shell-structured (or rattle-type) materials have attracted much attention for use in essential components of energy storage devices, as catalysts, and as sensors. These nanostructures have several advantages such as short Li^+ diffusion length, increased electrolyte–electrode contact area, and good tolerance to volume expansion and are therefore promising candidates as energy storage materials. Further, the core part of the yolk-shell powders increases the energy density and improves the rate performance of the battery materials. The use of yolk-shell-structured materials has previously been studied to improve the cycling performances and rate capacities of anode materials.[12−18]

Nickel oxide (NiO) is one of the promissing materials for use in LIBs because of its outstanding theoretical capacity (~ 718 mA h g^{-1}). However, nanostructured NiO materials prepared by conventional preparation processes show poor electrochemical performances.[19−24] In this regard, the characteristics of NiO yolk-shell powders with a well-defined morphology have not yet been studied.

Until now, the synthesis of the yolk-shell-structured materials required multiple steps and long processing times using techniques such as the etching technique, the technique involving the use of the Kirkendall effect, Ostwald ripening, and a soft templating process. In this study, we employed a continuous one-pot method of spray pyrolysis (Figure S1 of the Supporting Information) for the rapid synthesis of yolk-shell-structured NiO powders with high crystallinity for a few seconds. The electrochemical properties of the single-crystalline NiO nanopowders prepared by a continuous one-pot method via flame spray pyrolysis were also investigated (Figure S1 of the Supporting Information).

RESULTS AND DISCUSSION

The mechanisms of formation of yolk-shell and single-crystalline cubic NiO powders are shown in Figure 1. In both cases, several micrometer-sized droplets were fabricated by an ultrasonic nebulizer. In the spray pyrolysis process performed at the preparation temperature (900 °C), one yolk-shell-structured NiO particle was formed per droplet. A dense carbon–NiO intermediate was formed in the front part of the

Received: September 26, 2013
Accepted: February 3, 2014
Published: February 3, 2014

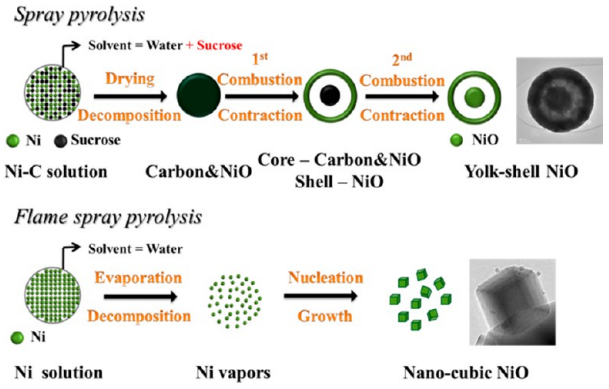

Figure 1. Schematic diagram of mechanisms of formation of the yolk-shell and single-crystalline cubic NiO powders by a one-pot gas phase reaction process.

horizontal-type reactor by the decomposition of nickel nitrate hexahydrate and the carbonization of sucrose. Combustion of the carbon–NiO intermediate produced the core-shell-structured carbon–NiO/NiO composite powder because of the incomplete combustion of the carbon component. The highly crystalline NiO shell formed by combustion of the carbon–NiO intermediate exhibited weak shrinking characteristics. However, contraction of the carbon–NiO core during further heating occurred, which yielded the carbon–NiO@void@NiO yolk-shell powder.[15] Subsequent combustion of the core part produced the final NiO yolk-shell powder with the distinctive NiO@void@NiO structure. Yolk-shell-structured NiO powders were prepared directly by spray pyrolysis. Single-crystalline NiO nanopowders exhibiting a cubic crystalline structure were prepared by flame spray pyrolysis at temperatures of >2500 °C. In this case, immediate drying of the droplet and decomposition of nickel nitrate produced the microsized NiO powders. Then, complete evaporation of the microsized NiO powders occurred inside the high-temperature diffusion flame over 2500 °C, thus yielding NiO vapors. NiO nuclei were formed by random collisions between the metal oxide molecules in the vapor state. Finally, single-crystalline NiO nanopowders were formed by the following sequential processes: nucleation, growth, and quenching.[25]

Transmission electron microscopy (TEM) images of the two types of NiO powders are shown in Figure 2. The low- and high-resolution TEM images of the yolk-shell-structured NiO powders are shown in panels a–c of Figure 2. The low-resolution TEM images clearly show the core and the single shell. The core size and shell thickness (Figure 2b) were 200 and 75 nm, respectively. The high-resolution TEM (HR-TEM) image (Figure 2c) shows well-developed crystals of the yolk-shell-structured powder prepared at a short residence time as stated above. The rapid exothermic decombustion of the carbon component comprising the carbon–NiO composite intermediate increased the temperature of the powder. Highly crystalline NiO yolk-shell-structured powders were prepared by one-pot method without post-treatment at high temperatures. The yolk-shell NiO powder directly prepared by spray pyrolysis exhibited clear lattice fringes separated by 0.24 nm, as shown in the HR-TEM image. This value corresponds to the (111) crystallographic plane of the cubic NiO.[24] The results of dot mapping (Figure S2 of the Supporting Information) confirm the single-shell structure of the NiO yolk-shell particle. The yolk-shell NiO particle showed a negligible carbon component in the dot mapping image. The carbon component completely combusted during the proces of the NiO yolk-shell particle. The TEM images of the single-crystalline cubic NiO nanopowders show regular hexahedral morphology (Figure 2d,e). The high formation temperature and the high cooling rate of the nanopowders produced a metastable polymorph. The HR-TEM images of the nanopowders exhibit clear lattice fringes separated by 0.24 nm and a single-crystalline structure (Figure 2f). The mean size and geometric standard deviation of the yolk-shell-structured NiO powders were 1 μm and 1.5, respectively. The HR-TEM images and selected-area electron diffraction (SAED) patterns of the core and shell parts were analyzed. The yolk-shell-structured NiO powders were crushed by hand for the TEM sample. The HR-TEM images and SAED patterns showed that the core and shell parts had similar morphologies and crystal structures. The carbon-like materials were not detected in the core part of the NiO yolk-shell-structured powder. The SAED patterns and energy-dispersive X-ray (EDS) spectrum analysis revealed that the obtained NiO yolk-shell powder had no impurities and exhibited a polycrystalline structure (Figure 3). The Brunauer–Emmett–Teller surface areas of the yolk-shell-structured and cubic NiO powders were 8 and 5 $m^2\ g^{-1}$, respectively. The X-ray diffraction (XRD) patterns of the two NiO powders matched the standard nickel oxide peaks (JCPDS 47-1049) (Figure S3 of the Supporting Information). The mean crystallite sizes of yolk-shell-structured and cubic NiO powders were 50 and 80 nm, respectively. The mean crystallite size of the cubic NiO nanopowders was similar to the mean size of the nanopowders measured from the TEM images.

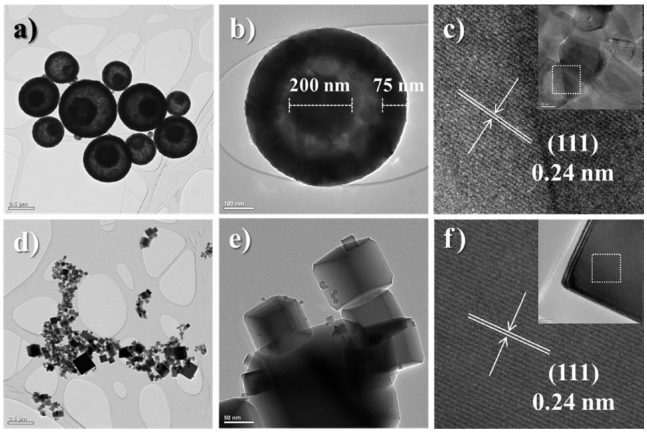

Figure 2. TEM images of yolk-shell and single-crystalline cubic NiO powders: (a–c) yolk-shell and (d–f) single-crystalline cubic.

Figure 4a shows the cyclic voltammetry (CV) curves of the electrodes made of the yolk-shell-structured and cubic NiO powders for the first three cycles at a scan rate of 0.07 mV s^{-1}. The faradic NiO reaction was NiO ↔ Ni/Li_2O in this voltage range.[23,24,26] One cathodic peak was observed at 0.6 V for the yolk-shell-structured NiO and at 0.3 V for the cubic NiO. The peak position difference of yolk-shell and cubic NiO powders during the first cathodic scan was related to the crystallite sizes and the charge-transfer resistances. Similar results for TiO_2 and Co_3O_4 systems have been reported.[27,28] Two broad oxidation NiO peaks for the oxidation of Ni nanograins to NiO and the subsequent decomposition of the SEI were observed.[22] The main reduction peaks shifted to ~1.2 V after the second cycle. The reduction and oxidation peaks in the CV tests substantially

dx.doi.org/10.1021/am404232x | ACS Appl. Mater. Interfaces 2014, 6, 2312–2316

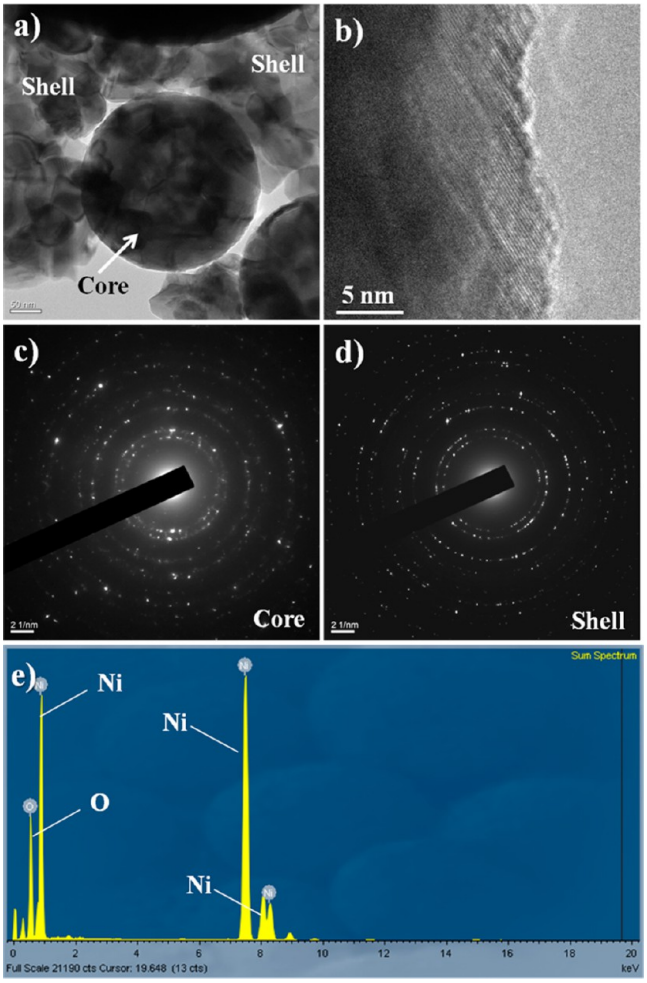

Figure 3. TEM images, SAED patterns, and EDS spectrum of the yolk-shell-structured NiO powders: (a) TEM images of core and shell parts, (b) HR-TEM image of the core part, (c) SAED pattern of the core part, (d) SAED pattern of the shell part, and (e) EDS spectrum of NiO powders.

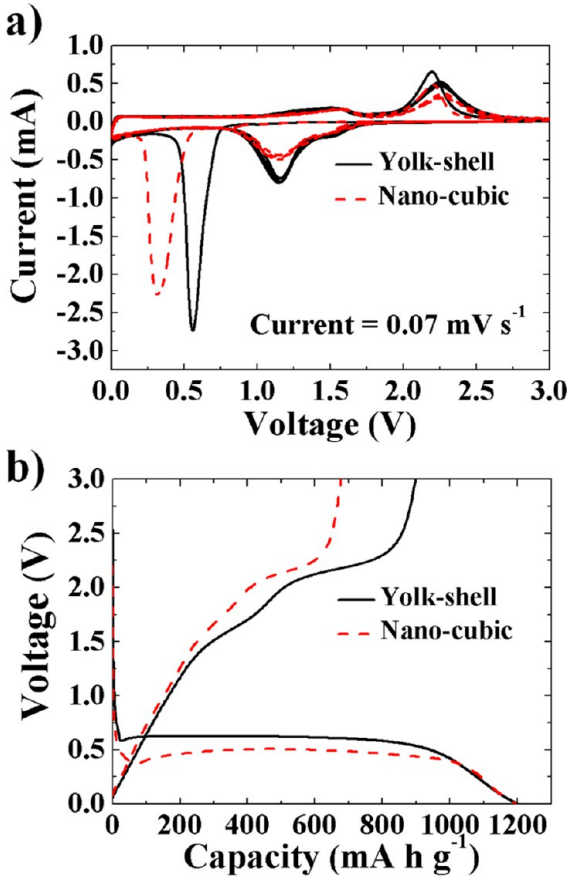

Figure 4. Electrochemical properties of the yolk-shell and single-crystalline cubic NiO powders: (a) Cyclic voltammograms of the first to third cycles at a scan rate of 0.07 mV s^{-1}, (b) Initial cycle profile in the voltage range of 0.001−3 V at 700 mA g^{-1}.

overlapped from the second cycle onward. Figure 4b shows the charge and discharge curves of the two types of NiO powders for the first cycles at a current density of 700 mA g^{-1}. The first discharge curves exhibit plateaus at ~0.55 and ~0.30 V for the yolk-shell-structured and cubic NiO powders, respectively. The wide potential plateau was replaced by a long slope between 1.3 and 0.5 V from the second cycle onward (Figure S4 of the Supporting Information). The yolk-shell-structured and single-crystalline cubic NiO powders exhibited similar initial discharge capacities of 1200 mA h g^{-1}. However, the initial charge capacities of the yolk-shell-structured and cubic NiO powders were 898 and 676 mA h g^{-1}, respectively, and their corresponding Coulombic efficiencies were 75 and 56%, respectively. The structural damage of the cubic NiO with large crystal sizes decreased the initial Coulombic efficiency in the first cycle. Figure 5a shows the cycle performances of the two types of NiO powders at a constant current density of 1 C between 0.001 and 3 V. The yolk-shell-structured and cubic NiO powders delivered discharge capacities of 951 and 416 mA h g^{-1}, respectively, after 150 cycles, and their corresponding capacity retentions measured after the first cycle were 106 and 66%, respectively. The discharge capacities of the yolk-shell NiO slightly decreased from 899 to 821 mA h g^{-1} from the second cycle over the first 60 cycles. After 60 cycles, the discharge capacities of the yolk-shell NiO increased gradually. The capacity increase during cycling for most transition-metal oxide anode materials has been well studied.[28−30] However, the single-crystalline cubic NiO nanopowders did not show any increase in discharge capacities after 150 cycles. Commonly, the formation of a polymeric gel-like film over the transition-metal oxides is promoted by small grain and particle sizes.[30]

The rate performances of the yolk-shell-structured and cubic NiO powders cycled at various current densities (increased stepwise from 200 mA g^{-1} to 1 A g^{-1} and then back to 200 mA g^{-1}) are shown in Figure 5b. The yolk-shell-structured and cubic NiO powders exhibited second discharge capacities of 1304 and 1260 mA h g^{-1}, respectively, at a low current density of 200 mA g^{-1}. The yolk-shell-structured NiO powders exhibited better rate performance than the cubic NiO nanopowders. The discharge capacity of the NiO yolk-shell powders was as high as 824 mA h g^{-1} after 50 cycles at a high current density of 1 A g^{-1}. Clearly, the decrease in the discharge capacity with an increase in current density was slower in the yolk-shell powders than in the cubic NiO nanopowders. The excellent rate performance of the yolk-shell-structured NiO powders was a direct result of the unique particle structure with a core@void@shell configuration, which reduced the lithium ion diffusion distance and facilitated rapid lithium ion diffusion. Figure 6 shows the TEM images of the anodes of the yolk-shell-structured and cubic NiO powders after 50 cycles in a fully charged state. Both samples exhibited a porous structure after

dx.doi.org/10.1021/am404232x | ACS Appl. Mater. Interfaces 2014, 6, 2312−2316

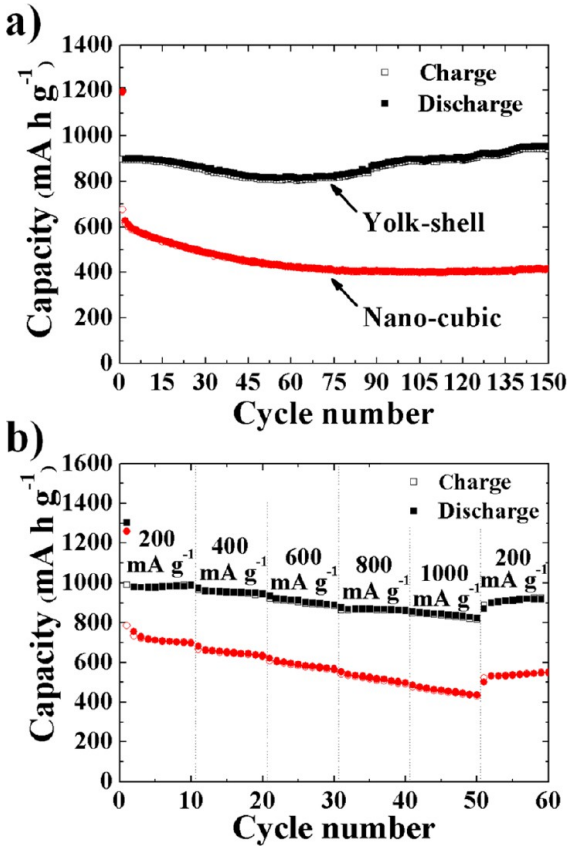

Figure 5. Cycle properties of the yolk-shell and single-crystalline cubic NiO powders in the voltage range of 0.001−3 V: (a) Cycle performances at 700 mA g^{-1}, (b) Rate performances at various currents.

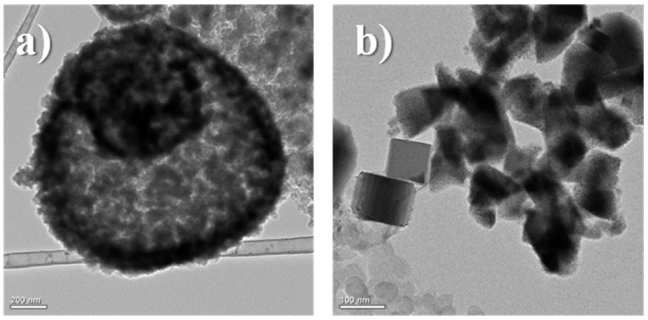

Figure 6. TEM images of the yolk-shell (a) and single-crystalline cubic (b) NiO powders after the 50th cycle with a fully charged state.

cycling. The yolk-shell-structured NiO powders maintained their overall morphology after cycling, but the cubic NiO nanopowders nearly lost their original morphology, as shown in panels a and b of Figure 6. The Nyquist impedance plots obtained before cycling and after 50 cycles are shown in panels a and b of Figure 7, respectively. The semicircle diameter obtained before cycling in the medium-frequency region for the cubic NiO was slightly larger than that in the case of the yolk-shell NiO, as shown in Figure 7a. The charge-transfer resistance (R_{ct}) of the cubic NiO electrode was larger than that of the yolk-shell-structured NiO electrode because of the former's larger grain and particle sizes. Furthermore, the same semicircle diameter for the yolk-shell NiO electrode was maintained after cycling. In contrast, the semicircle diameter for the cubic NiO

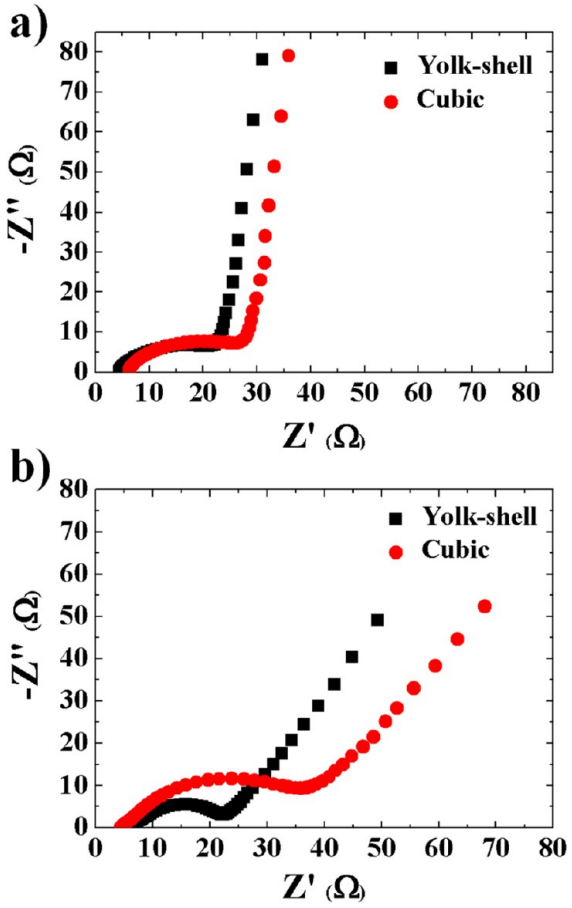

Figure 7. Nyquist impedance plots of the yolk-shell and single-crystalline cubic NiO powders (a) before cycling and (b) after the 50th cycle with a fully charged state.

increased after cycling. The cycling-induced structural destruction of the cubic NiO nanopowders with large mean crystallite sizes decreased the cycling performance. Poizot et al. demonstrated that transition-metal oxides showed good electrochemical properties at a certain optimal particle size.[1] The yolk-shell-structured NiO powders with a small crystallite size showed high initial charge and discharge capacities and high capacity retention because of their structural stability during cycling. The peculiar structure of the yolk-shell NiO powders with a core@void@shell configuration also improved the structural stability during cycling.

CONCLUSIONS

In summary, the electrochemical properties of the NiO yolk-shell powders prepared by the one-pot method as an anode material for LIBs were compared to those of the single-crystalline cubic NiO nanopowders prepared by high-temperature (>2500 °C) flame spray pyrolysis. Repeated combustion and contraction of the carbon−NiO composite formed as an intermediate inside the reactor maintained at 900 °C produced the NiO yolk-shell powder with a distinctive NiO@void@NiO structure. Single-crystalline NiO nanopowders with a cubic crystalline lattice structure were formed directly from the NiO vapors by nucleation, growth, and subsequent quenching. The structural destruction of the cubic NiO nanopowders with a large mean crystallite size (80 nm) from the first cycle resulted in an irreversible, high initial capacity loss during the first cycle

dx.doi.org/10.1021/am404232x | ACS Appl. Mater. Interfaces 2014, 6, 2312−2316

and poor cycling performance thereafter. However, the yolk-shell-structured NiO powders with a small crystallite size (50 nm) showed higher capacities and good capacity retention even at a high current density of 1000 mA g^{-1} because of their excellent structural stability.

EXPERIMENTAL SECTION

Synthesis of Yolk-Shell and Single-Crystalline Cubic NiO Powders. Yolk-shell-structured and single-crystalline cubic NiO powders were directly prepared by spray pyrolysis and flame spray pyrolysis, respectively, from their corresponding aqueous spray solutions. A schematic diagram of the ultrasonic spray pyrolysis system used for the NiO yolk-shell-structured powders is shown in Figure S1a of the Supporting Information. An aqueous spray solution was prepared using nickel nitrate hexahydrate [$Ni(NO_3)_2{\cdot}6H_2O$ (Junsei)]. The concentrations of aqueous solutions of nickel nitrate hexahydrate and sucrose were 0.2 and 0.7 M, respectively. A schematic diagram of the flame spray pyrolysis system used for the preparation of single-crystalline NiO nanopowders exhibiting a cubic crystalline lattice structure is depicted in Figure S1b of the Supporting Information. A detailed structure of the flame spray pyrolysis system was presented in our previous work.[25]

Characterizations. The crystal structures of the NiO powders were investigated by X-ray diffraction (X'pert PRO MPD) using Cu Kα radiation (λ = 1.5418 Å) at the Korea Basic Science Institute (Daegu, Korea). Morphological characteristics were investigated using HR-TEM (JEOL-2100F) at a working voltage of 200 kV. The specific surface area of the NiO powders with various shapes was calculated using Brunauer–Emmett–Teller (BET) analysis of nitrogen adsorption (TriStar 3000). The experimental description for electrochemical measurements of the powders was previously described.[31]

ASSOCIATED CONTENT

Supporting Information

Schematic diagram of the spray pyrolysis process, dot mapping images, XRD patterns, initial charge and discharge curves of the yolk-shell-structured and single-crystalline cubic NiO powders, cycle performance at an operating temperature of 60 °C, SEM images of the yolk-shell-structured NiO powders before and after cycling, SEM images of the NiO powders prepared under various conditions, and nitrogen adsorption–desorption isotherms. This material is available free of charge via the Internet at http://pubs.acs.org.

AUTHOR INFORMATION

Corresponding Author

*Telephone: +82-2-2049-6010. Fax: +82-2-458-3504. E-mail: yckang@konkuk.ac.kr.

Notes

The authors declare no competing financial interest.

ACKNOWLEDGMENTS

This work was supported by a National Research Foundation of Korea (NRF) grant funded by the Korea government (MEST) (2012R1A2A2A02046367), the Converging Research Center Program through the National Research Foundation of Korea (NRF) funded by the Ministry of Education, Science and Technology (2011-50210), and the Creative Industrial Technology Development Program (10045141) funded by the Ministry of Trade, Industry & Energy.

REFERENCES

(1) Poizot, P.; Laruelle, S.; Grugeon, S.; Dupont, L.; Tarascon, J. M. *Nature* **2000**, *28*, 496–499.
(2) Wang, Z. Y.; Zhou, L. A.; Lou, X. W. *Adv. Mater.* **2012**, *24*, 1903–1911.
(3) Wang, H. L.; Cui, L. F.; Yang, Y.; Casalongue, H. S.; Robinson, J. T.; Liang, Y. Y.; Cui, Y.; Dai, H. J. *J. Am. Chem. Soc.* **2010**, *132*, 13978–13980.
(4) Wu, H. B.; Chen, J. S.; Hng, H. H.; Lou, X. W. *Nanoscale* **2012**, *4*, 2526–2542.
(5) Jia, X.; Chen, Z.; Cui, X.; Peng, Y.; Wang, X.; Wang, G.; Wei, F.; Lu, Y. *ACS Nano* **2012**, *6*, 9911–9919.
(6) Choi, N. S.; Yao, Y.; Cui, Y.; Cho, J. P. *J. Mater. Chem.* **2011**, *21*, 9825–9840.
(7) Zhang, W. M.; Hu, J. S.; Guo, Y. G.; Zheng, S. F.; Zhong, L. S.; Song, W. G.; Wan, L. J. *Adv. Mater.* **2008**, *20*, 1160–1165.
(8) Park, M. S.; Wang, G. X.; Kang, Y. M.; Wexler, D.; Dou, S. X.; Liu, H. K. *Angew. Chem., Int. Ed.* **2007**, *46*, 750–753.
(9) Xie, Q. S.; Li, F.; Guo, H. Z.; Wang, L. S.; Chen, Y. Z.; Yue, G. H.; Peng, D. L. *ACS Appl. Mater. Interfaces* **2013**, *5*, 5508–5517.
(10) Park, J. C.; Kim, J. H.; Kwon, H. S.; Song, H. J. *Adv. Mater.* **2009**, *21*, 803–807.
(11) Dai, Yi. H.; Jiang, H.; Hu, Y. J.; Li, C. Z. *RSC Adv.* **2013**, *3*, 19778–19781.
(12) Liu, R.; Yang, S. C.; Wang, F.; Lu, X. G.; Yang, Z. M.; Ding, B. J. *ACS Appl. Mater. Interfaces* **2012**, *4*, 1537–1542.
(13) Zhang, G. Q.; Yu, L.; Wu, H. B.; Hoster, H. E.; Lou, X. W. *Adv. Mater.* **2012**, *24*, 4609–4613.
(14) Liu, J.; Qiao, S. Z.; Chen, J. S.; Lou, X. W.; Xing, X. R.; Lu, G. Q. *Chem. Commun.* **2011**, *47*, 12578–12591.
(15) Hong, Y. J.; Son, M. Y.; Kang, Y. C. *Adv. Mater.* **2013**, *25*, 2279–2283.
(16) Lou, X. W.; Deng, D.; Lee, J. Y.; Archer, L. A. *Chem. Mater.* **2008**, *20*, 6562–6566.
(17) Chen, J. S.; Li, C. M.; Zhou, W. W.; Yan, Q. Y.; Archer, L. A.; Lou, X. W. *Nanoscale* **2009**, *1*, 280–285.
(18) Lou, X. W.; Archer, L. A.; Yang, Z. *Adv. Mater.* **2008**, *20*, 3987–4019.
(19) Oh, S. W.; Bang, H. J.; Bae, Y. C.; Sun, Y. K. *J. Power Sources* **2007**, *173*, 502–509.
(20) Varghese, B.; Yanwu, M. V. Z.; Lit, C. S.; Hoong, T. C.; Rao, G. V. S.; Chowdari, B. V. R.; Wee, A. T. S.; Lim, C. T.; Sow, C. H. *Chem. Mater.* **2008**, *20*, 3360–3367.
(21) Cha, H. G.; Sohn, J. H.; Park, Y. J.; Lee, K. J.; Jung, M. H.; Lee, J. W.; Shin, W. S.; Kang, M. J.; Kim, D. Y.; Kang, Y. S. *RSC Adv.* **2012**, *2*, 9786–9790.
(22) Su, D. W.; Ford, M.; Wang, G. X. *Sci. Rep.* **2012**, *2*, 924.
(23) Huang, X. H.; Tu, J. P.; Zhang, C. Q.; Xiang, J. Y. *Electrochem. Commun.* **2007**, *9*, 1180–1184.
(24) Mai, Y. J.; Shi, S. J.; Zhang, D.; Lu, Y.; Gu, C. D.; Tu, J. P. *J. Power Sources* **2012**, *204*, 155–161.
(25) Choi, S. H.; Kang, Y. C. *Nanoscale* **2013**, *5*, 4662–4668.
(26) Rahman, M. M.; Chou, S. L.; Zhong, C.; Wang, J. Z.; Wexler, D.; Liu, H. K. *Solid State Ionics* **2010**, *180*, 1646–1651.
(27) Subramanian, V.; Karki, A.; Gnanasekar, K. I.; Eddy, F. P.; Rambabu, B. *J. Power Sources* **2006**, *159*, 186–192.
(28) Wu, Z. S.; Ren, W. C.; Wen, L.; Gao, L. B.; Zhao, J. P.; Chen, Z. P.; Zhou, G. M.; Li, F.; Cheng, H. M. *ACS Nano* **2010**, *4*, 3187–3194.
(29) Zhou, G. M.; Wang, D. W.; Li, F.; Zhang, L. L.; Li, N.; Wu, Z. S.; Wen, L.; Lu, G. Q.; Cheng, H. M. *Chem. Mater.* **2010**, *22*, 5306–5313.
(30) Do, J. S.; Weng, C. H. *J. Power Sources* **2005**, *146*, 482–486.
(31) Choi, S. H.; Kang, Y. C. *ChemSusChem* **2013**, *6*, 2111–2116.